

A polarimetrically oriented X-ray stare at the accreting pulsar EXO 2030+375

Christian Malacaria¹, Jeremy Heyl², Victor Doroshenko³, Sergey S. Tsygankov⁴, Juri Poutanen⁴, Sofia V. Forsblom⁴, Fiamma Capitanio⁵, Alessandro Di Marco⁵, Yujia Du³, Lorenzo Ducci^{3,6}, Fabio La Monaca⁵, Alexander A. Lutovinov⁷, Herman L. Marshall⁸, Ilya A. Mereminskiy⁷, Sergey V. Molkov⁷, Alexander A. Mushtukov⁹, Mason Ng⁸, Pierre-Olivier Petrucci¹⁰, Andrea Santangelo³, Andrey E. Shtykovsky⁷, Valery F. Suleimanov³, Iván Agudo¹¹, Lucio A. Antonelli^{12,13}, Matteo Bachetti¹⁴, Luca Baldini^{15,16}, Wayne H. Baumgartner¹⁷, Ronaldo Bellazzini¹⁵, Stefano Bianchi¹⁸, Stephen D. Bongiorno¹⁷, Raffaella Bonino^{19,20}, Alessandro Brez¹⁵, Niccolò Bucciantini^{21,22,23}, Simone Castellano¹⁵, Elisabetta Cavazzuti²⁴, Chien-Ting Chen²⁵, Stefano Ciprini^{26,13}, Enrico Costa⁵, Alessandra De Rosa⁵, Ettore Del Monte⁵, Laura Di Gesu²⁴, Niccolò Di Lalla²⁷, Immacolata Donnarumma²⁴, Michal Dovčiak²⁸, Steven R. Ehlert¹⁷, Teruaki Enoto²⁹, Yuri Evangelista⁵, Sergio Fabiani⁵, Riccardo Ferrazzoli⁵, Javier A. Garcia³⁰, Shuichi Gunji³¹, Kiyoshi Hayashida^{32,†}, Wataru Iwakiri³³, Svetlana G. Jorstad^{34,35}, Philip Kaaret¹⁷, Vladimir Karas²⁸, Fabian Kislat³⁶, Takao Kitaguchi²⁹, Jeffery J. Kolodziejczak¹⁷, Henric Krawczynski³⁷, Luca Latronico¹⁹, Ioannis Liodakis³⁸, Simone Maldera¹⁹, Alberto Manfreda³⁹, Frédéric Marin⁴⁰, Andrea Marinucci²⁴, Alan P. Marscher³⁴, Francesco Massaro^{19,20}, Giorgio Matt¹⁸, Ikuyuki Mitsuishi⁴¹, Tsunefumi Mizuno⁴², Fabio Muleri⁵, Michela Negro^{43,44,45}, Chi-Yung Ng⁴⁶, Stephen L. O'Dell¹⁷, Nicola Omodei²⁷, Chiara Oppedisano¹⁹, Alessandro Papitto¹², George G. Pavlov⁴⁷, Abel L. Peirson²⁷, Matteo Perri^{13,12}, Melissa Pesce-Rollins¹⁵, Maura Pilia¹⁴, Andrea Possenti¹⁴, Simonetta Puccetti¹³, Brian D. Ramsey¹⁷, John Rankin⁵, Ajay Ratheesh⁵, Oliver J. Roberts²⁵, Roger W. Romani²⁷, Carmelo Sgrò¹⁵ Patrick Slane⁴⁸, Paolo Soffitta⁵, Gloria Spandre¹⁵, Douglas A. Swartz²⁵, Toru Tamagawa²⁹, Fabrizio Tavecchio⁴⁹, Roberto Taverna⁵⁰, Yuzuru Tawara²⁶, Allyn F. Tennant¹⁷, Nicholas E. Thomas¹⁷, Francesco Tombesi^{51,26,52}, Alessio Trois¹⁴, Roberto Turolla^{50,53}, Jacco Vink⁵⁴, Martin C. Weisskopf¹⁷, Kinwah Wu⁵³, Fei Xie^{55,5}, and Silvia Zane⁵³

(Affiliations can be found after the references)

Received 3 April 2023 / Accepted 10 May 2023

ABSTRACT

Accreting X-ray pulsars (XRPs) are presumed to be ideal targets for polarization measurements, as their high magnetic field strength is expected to polarize the emission up to a polarization degree of \sim 80%. However, such expectations are being challenged by recent observations of XRPs with the Imaging X-ray Polarimeter Explorer (IXPE). Here, we report on the results of yet another XRP, namely, EXO 2030+375, observed with IXPE and contemporarily monitored with Insight-HXMT and SRG/ART-XC. In line with recent results obtained with IXPE for similar sources, an analysis of the EXO 2030+375 data returns a low polarization degree of 0%–3% in the phase-averaged study and a variation in the range of 2%–7% in the phase-resolved study. Using the rotating vector model, we constrained the geometry of the system and obtained a value of \sim 60° for the magnetic obliquity. When considering the estimated pulsar inclination of \sim 130°, this also indicates that the magnetic axis swings close to the observer's line of sight. Our joint polarimetric, spectral, and timing analyses hint toward a complex accreting geometry, whereby magnetic multipoles with an asymmetric topology and gravitational light bending significantly affect the behavior of the observed source.

Key words. magnetic fields – polarization – stars: neutron – X-rays: binaries – pulsars: individual: EXO 2030+375

1. Introduction

Accreting X-ray pulsars (XRPs) are binary systems consisting of a neutron star (NS) and a donor companion star (see Mushtukov & Tsygankov 2022, for a recent review). In these systems, the NS can accrete matter supplied by the companion either via stellar wind or Roche-lobe overflow, thereby poducing emission in the X-ray domain. The NS can be strongly magnetized, with a dipolar magnetic field strength on the order of 10^{12} G. This leads to highly anisotropic accretion, where

the matter is funneled by the magnetic field to the magnetic poles, giving rise to pulsating X-ray emission. Studying these systems is crucial for understanding the effects related to the interaction of X-ray radiation with strongly magnetized plasma. In fact, the emission from XRPs can be expected to be strongly polarized, up to a polarization degree (PD) of 80% due to magnetized plasma and vacuum birefringence (Gnedin et al. 1978; Pavlov & Shibanov 1979; Meszaros et al. 1988; Caiazzo & Heyl 2021b,a). However, recent observations of XRPs have revealed a polarization that is far lower than expected (Doroshenko et al. 2022; Tsygankov et al. 2022; Forsblom et al. 2023), with a

[†] Deceased.

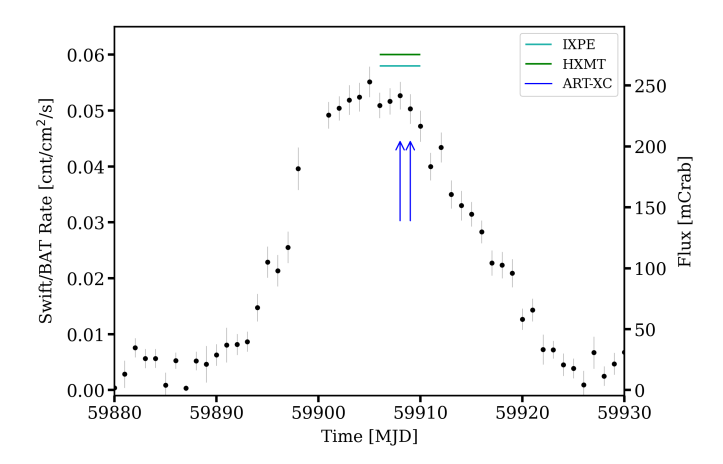


Fig. 1. *Swift/BAT* (15–50 keV) daily average light curve of EXO 2030+375 (black dots with gray error bars). Times of each continuous and pointed observations used in this work are marked by horizontal colored lines and vertical arrows, as detailed in the legend.

phase-averaged PD of about 5%-6% and ranging from 5% to 15% in the phase-resolved analysis.

EXO 2030+375 is an XRP discovered with the EXOSAT observatory (Parmar et al. 1989), which also detected pulsations at about 42 s. The orbital period of 46.02 days was derived from the Type I outburst periodicity by Wilson et al. (2008). These authors also obtained an orbital solution consisting of a rather eccentric (eccentricity of $e \sim 0.41$) and wide (semi-major axis of $a_x \sin i = 248 \pm 2 \text{ lt-s}$) orbit. Besides being the most regular and prolific Type I outburst XRP, EXO 2030+375 also has shown sporadic Type II (or giant) outbursts (Parmar et al. 1989; Corbet & Levine 2006; Thalhammer et al. 2021). The source spectrum showed a hint of the cyclotron resonant scattering feature (CRSF) at 36 keV (Reig & Coe 1998) and 63 keV (Klochkov et al. 2008), however, this has not been securely confirmed in other works. More recently, the source spin period was measured to be around 41.2 s (Thalhammer et al. 2021), after the source underwent a significant spin-up episode following the Type II outburst, as monitored by Fermi/GBM¹. The distance to the source is $2.4^{+0.5}_{-0.4}$ kpc, as given in the *Gaia* Data Release 3 (Bailer-Jones et al. 2021).

Here, we present the results of a multi-observatory campaign on EXO 2030+375. The observations by the Imaging X-ray Polarimeter Explorer (IXPE) were supplemented by contemporaneous observations with Insight-HXMT and Spectrum-Roentgen-Gamma/ART-XC at the peak of a Type I outburst in 2022.

2. Observations and data reduction

2.1. IXPE

IXPE (Weisskopf et al. 2022) is a NASA small explorer mission in collaboration with the Italian Space Agency (ASI), launched on 2021 December 9. It features three identical Mirror Module Assembly (MMAs), each comprising of a grazing incidence telescope and a polarization-sensitive Detector Unit (DU) at its focus (Baldini et al. 2021; Soffitta et al. 2021). The DUs consist of gas-pixel detectors (GPD) filled with dimethyl ether, whose interaction with X-ray photons produces photoelectrons that are ejected in a direction that is distributed

as $\cos^2 \varphi$, where φ is the polarization direction of the incident radiation (Bellazzini & Angelini 2003). IXPE provides imaging polarimetry over a nominal energy band of 2–8 keV, within a field of view of about 12.9 arcmin² for each MMA and with an energy-dependent polarization sensitivity expressed by a modulation factor (i.e., the amplitude of the instrumental response to 100% polarized radiation) peaking at $\mu \sim 50\%$ –60% at 8 keV.

IXPE observed EXO 2030+375 over the period 2022 November 23–27 (ObsID 02250201) for a total exposure of about 181 ks. A *Swift*/BAT (Gehrels et al. 2004; Krimm et al. 2013) light curve of the relevant outburst with IXPE and other pointed observations is shown in Fig. 1. IXPE data have been reduced using the IXPEOBSSIM software package (Baldini et al. 2022), version 30.0.0², and using the CALDB version 20221020. Source events were extracted from a 60" radius circle centered on the brightest pixel, while background events are negligible given the relatively high source count rate (Di Marco et al. 2023). The v12 version of the weighted response files (Di Marco et al. 2022) was used to produce and analyze spectral products. Based on Silvestri (2023), we added a systematic error of 2% to the IXPE spectra.

2.2. SRG/ART-XC

The Mikhail Pavlinsky ART-XC telescope (Pavlinsky et al. 2021) carried out two consecutive observations (ObsIDs: 12210071001, 12210071002) of EXO 2030+375, from 2022 November 25–26 (MJD 59908.87-59909.62 and 59909.71-59909.83), simultaneously with IXPE, with a total net exposure of 75 ks. ART-XC is a grazing incidence-focusing X-ray telescope on board the SRG observatory (Sunyaev et al. 2021). The telescope includes seven independent modules and provides imaging, timing, and spectroscopy in the 4–30 keV energy range, with a total effective area of ~450 cm² at 6 keV, angular resolution of 45", energy resolution of 1.4 keV at 6 keV, and timing resolution of 23 µs. The ART-XC data were processed with the software ARTPRODUCTS v1.0 and the CALDB version 20230228. We limited the ART-XC energy band to the 6.5–25 keV energy range, where the instrument calibration is better known. Following standard procedures, we merged data from both observations, rebinned the spectrum to match the energy resolution of the detectors, and added a systematic error of 2% to it.

2.3. Insight-HXMT

Hard X-ray Modulation Telescope (HXMT, also dubbed as Insight-HXMT) excels in its broad energy band (1–250 keV) and a large effective area in the hard X-ray energy band (Zhang et al. 2020). EXO 2030+375 was observed by HXMT from 2022 November 18 (MJD 59901) to November 27 (MJD 59910). In this work, we only analyze quasi-simultaneous observations with IXPE from 2022 November 23 (MJD 59905) to November 27 (MJD 59910). The resulting total exposure times are 42 ks, 71 ks and 67 ks for the detectors of three payloads on board HXMT, LE (1–15 keV), ME (5–30 keV), and HE (20–250 keV), respectively. The detectors were used to generate the events in good time intervals (GTIs). The time resolution of the HE, ME, and LE instruments are \sim 25 μ s, \sim 280 μ s, and \sim 1 ms, respectively. Data from HXMT were considered in the range 2-70 keV, with the exclusion of 21-24 keV data due to the presence of an Ag feature (Li et al. 2020). Insight-HXMT Data Analysis software

https://gammaray.nsstc.nasa.gov/gbm/science/pulsars/ lightcurves/exo2030.html

https://github.com/lucabaldini/ixpeobssim

http://hxmtweb.ihep.ac.cn/

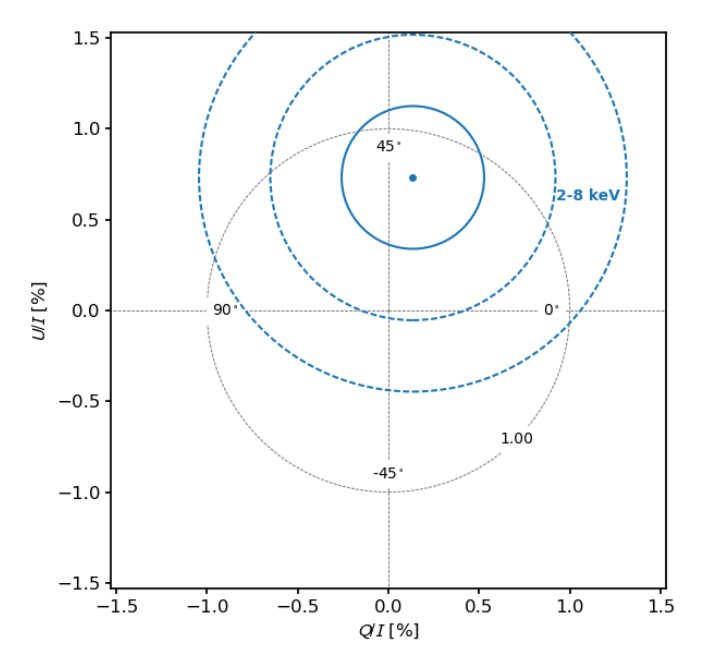


Fig. 2. Pulse phase-averaged normalized Stokes parameters U/I (y-axis) and Q/I (x-axis) over the 2–8 keV energy range. The 1σ , 2σ , and 3σ contours are plotted as concentric circles around the nominal value (continuous and dashed lines, respectively). The gray dotted circle represents loci of constant 1% PD, while radial lines are labeled for specific electric vector position angles (that is, the polarization angle, PA) with respect to north. The phase-averaged PD upper limit is about 2% at 99% c.l.

(HXMTDAS) v2.05 and HXMTCALDB v2.05 are used to analyze the data. We screened events for three payloads in HXMTDAS using legtigen, megtigen, hegtigen tasks according to the following criteria for the selection of GTIs: (1) pointing offset angle $<0.1^{\circ}$; (2) the elevation angle $>10^{\circ}$; (3) the geomagnetic cut-off rigidity >8 GeV; (4) the time before and after the South Atlantic Anomaly passage >300 s; (5) for LE observations, pointing direction above bright Earth >30°. We selected events from the small field of views (FoVs) for LE and ME observations, and from both small and large FoVs for HE observations due to the limitation of the background calibration. The instrumental background is estimated by blocking the collimators of some detectors completely. The background model is developed by taking the correlations of the count rates between the blind and other detectors. The background is generated with lebkgmap, mebkgmap, and hebkgmap implemented in HXMTDAS, respectively. We restricted the energy band for spectral analysis to 1-10, 10-30, and 30-70 keV for LE, ME, and HE, respectively, as these ranges suffer smaller calibration uncertainties given the available observational background. Following the official team recommendations, we added a systematic error of 1% to LE and ME spectra, and 3% to the HE spectrum.

3. Data analysis and results

Polarimetric parameters were derived following the approach based on the formalism by Kislat et al. (2015), as implemented in the pcube software algorithm and through spectropolarimetric analysis available in XSPEC (Strohmayer 2017). The spectra were fitted simultaneously in XSPEC allowing for a cross-calibration constant to account for calibration uncertainties of different DUs with respect to other detectors and for intrinsic

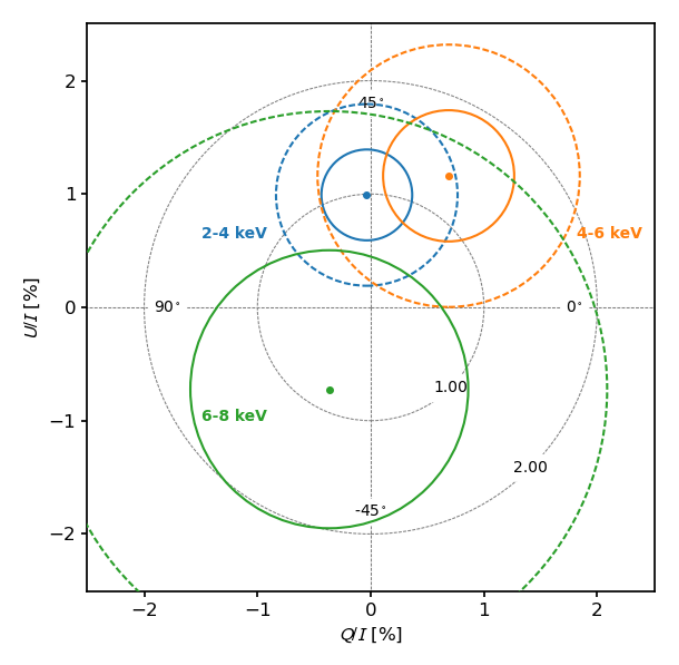


Fig. 3. Same details as in Fig. 2 for energy-dependent normalized Stokes parameters. Gray dotted circles represents loci of constant 1% and 2% PD. Blue, orange, and green circles represent the 2–4, 4–6 and 6–8 keV energy bands, respectively.

source variability. The source spectra were rebinned to have at least 30 counts per energy channel in order to adopt the χ^2 fit statistic, given the non-Poissonian nature of the source spectra. The adopted test statistic was the χ^2 . Spectral data were analyzed with XSPEC version 12.13.0b (Arnaud 1996) available with HEASOFT v6.31.

3.1. Timing analysis

Barycentric correction was applied to the events using the barycorr tool for IXPE and ART-XC, and the HXMTDAS task hxbary for HXMT. DE421 Solar system ephemeris and the SIMBAD (Wenger et al. 2000) ICRS coordinates of the source were employed to this aim. Binary demodulation also was performed, employing the orbital solution from Fu et al. (2023). The final estimate of the spin period $P_{\rm s} = 41.1187(1)\,{\rm s}$ was then obtained using the phase connection technique (Deeter et al. 1981) and HXMT/LE events. The obtained spin period was used to fold the events from all employed instruments and obtain corresponding pulse profiles.

For completeness, we also extracted the IXPE light curve in the 2–8 keV energy band summed over the three DUs and rebinned at 300 s. The resulting light curve shows a steady count rate of about 5 cnt $\rm s^{-1}$ over the whole IXPE observation.

3.2. Phase-averaged analysis

3.2.1. Phase-averaged polarimetric analysis

Polarization quantities were initially derived following the model-independent approach described in Kislat et al. (2015) and Baldini et al. (2022). Normalized Stokes parameters, Q/I and U/I, were extracted using the pcube algorithm within IXPEOBSSIM and then used to obtain the PD and PA. Figure 2 shows those parameters for the full 2–8 keV energy band, while Fig. 3 shows the same in different energy bands. Both plots show

Table 1. Best-fit parameters of the phase-averaged IXPE data on EXO 2030+375 obtained from spectro-polarimetric analysis using model const×tbabs(powerlaw×polconst) in the 2-8 keV energy band.

Parameter	Value		
$C_{\rm DU1}$ (fixed)	1		
$C_{ m DU2}$	0.963 ± 0.003		
$C_{ m DU3}$	0.928 ± 0.003		
$N_{\rm H} [10^{22} {\rm cm}^{-2}]$	1.93 ± 0.06		
Γ	1.29 ± 0.01		
Norm (a)	0.315 ± 0.006		
PD [%]	1.2 ± 0.4		
PA [deg]	39 ± 9		
$Flux_{2-10keV}$ (b)	2.47 ± 0.05		
χ^2 /d.o.f.	1372/1334		

Notes. All reported errors are at the 68% confidence level and based on the MCMC chain values. ^(a)Normalization of the power law in units of photon keV⁻¹ cm⁻² s⁻¹ at 1 keV. ^(b)Unabsorbed flux calculated for the entire model (in units of 10^{-9} erg cm⁻² s⁻¹), obtained using the cflux model from XSPEC as resulting from DU1.

that the normalized Stokes parameters are consistent with zero, which implies that the PD is also consistent with zero and is lower than $\sim 3\%$ at 99% c.l.

3.2.2. Phase-averaged spectro-polarimetric analysis

To perform the spectro-polarimetric analysis, we first limited the study to IXPE data only. The I, Q, and U spectra from the source were extracted using the xpbin algorithm for each DU. Given the narrow energy range of IXPE data, the spectra can be fitted with a simpler model than that required for broaderband analysis. We therefore employed a simple absorbed power-law model for the IXPE-only analysis. A constant polarization component (energy-independent PD and PA) was also added to the model in XSPEC. The final form of the model was thus const×tbabs(powerlaw×polconst). This model returns a fit-statistic χ^2 /d.o.f. = 1372/1334 (see Table 1 and Fig. 4). Errors are calculated through MCMC simulations using the Goodman-Weare algorithm of length 2×10^5 with 20 walkers and 10^4 burn-in steps. Best-fit results are shown in Table 1. The analysis reveals a PD of $1.2 \pm 0.6\%$ at the 90% c.1.

To test a possible energy-dependence of the polarization properties in EXO 2030+375, different polarization model components were also tested, namely pollin and polpow in XSPEC, corresponding to a linear and a power-law dependence with energy, respectively, of the PD and PA. However, these models did not further reduce the χ^2 value, nor returned significantly different polarimetric quantities and were, therefore, not explored further.

Finally, we simultaneously fitted IXPE, HXMT, and ART-XC spectra. In principle, with a broadband spectrum available, polarimetric results suffer less contamination from a possibly incorrect spectral model derived by the restricted IXPE energy band. Following previous works (Klochkov et al. 2008; Epili et al. 2017; Fürst et al. 2018; Tamang et al. 2022), we adopted an absorbed power-law model with high-energy cutoff and an iron $K\alpha$ line. To this, we added a constant polarization component as above. As the iron line is produced by fluorescence, it is not expected to be polarized. We verified this by adding a separate polconst component for the

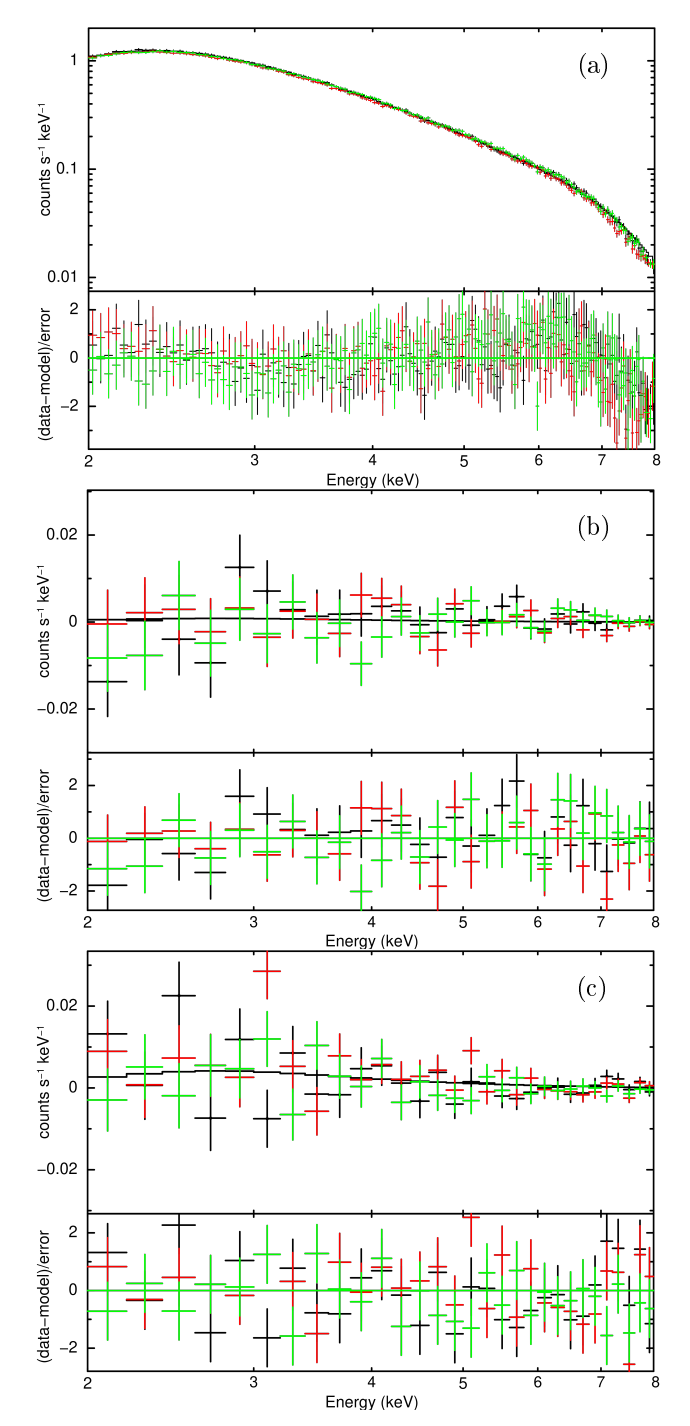


Fig. 4. EXO 2030+375 spectral energy distribution of the phase-averaged Stokes parameters I, Q, and U as observed by IXPE – panels (a), (b), and (c), respectively. Continuous lines in the top panels represent the best-fit model const×tbabs(powerlaw×polconst) reported in Table 1. Bottom panels show the residuals. Different colors represent different detectors – black for DU1, red for DU2, and green for DU3. Data have been rebinned and re-normalized for plotting purpose.

continuum and for the iron line. This resulted in a best-fit model whose PD value for the iron line was pegged at its lower limit. Therefore, we left that component unaffected by polarization. The final model expression is thus const×tbabs (powerlaw×highecut×polconst+gauss). For the fitting procedure, IXPE and SRG/ART-XC spectral parameters were tied to those from HXMT/LE, leaving a cross-calibration

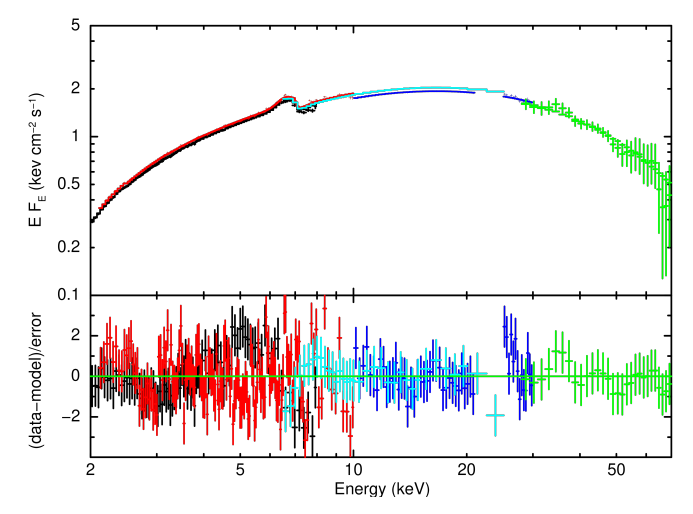


Fig. 5. Phase-averaged broadband spectrum of EXO 2030+375. Top: EXO 2030+375 unfolded EF_E spectrum as observed by IXPE, HXMT, and ART-XC. For plotting purpose, data from the three IXPE DUs are combined and re-normalized, and all spectra are rebinned. IXPE data are in red, HXMT LE, ME, and HE in black, blue and green, respectively, ART-XC data are in cyan. Bottom: residuals of the best-fit model (also see Table 2).

constant free for each instrument. For the photoelectric absorption from neutral interstellar matter, we employed the tbabs model from Wilms et al. (2000) and relative wilm abundances. The Galactic column density in the direction of the source is about $8.8 \times 10^{21} \, \mathrm{cm}^{-2}$ (HI4PI Collaboration 2016).

Despite the more elaborate model (with respect to the IXPE-only analysis) and the broad 2–70 keV energy band, we were still able to verify that the obtained best-fit values of the PD and PA are in agreement with those reported in Sect. 3.2.1 within 1σ . The broadband spectral results are shown in Fig. 5 and reported in Table 2.

3.3. Phase-resolved (spectro-)polarimetric analysis

To perform a phase-resolved polarization analysis of IXPE data, we selected seven phase bins to sample different flux levels shown by the pulse profile (see Fig. 6). The phase bins were extracted with respect to $T_0 = 59906.82181991$ MJD.

For the polarimetric analysis, we followed the Kislat et al. (2015) formalism as outlined in Sect. 3.2.1. The results, shown in Fig. 6, exhibit only a moderate variability of the Stokes parameters as a function of the pulse phase.

To perform the spectro-polarimetric analysis of the phase-resolved spectra, we used the same model as we did for the phase-averaged analysis in Sect. 3.2.2. Phase-resolved spectra were rebinned analogously to the phase-averaged analysis. For IXPE, cross-normalization constants were kept fixed at their correspondent phase-averaged value (see Table 1). The resulting best-fit values are reported in Table 3 and shown in Fig. 6. The analysis reveals significant detection of polarization up to about 7%. Both the PD and PA show pronounced variation with spin phase.

3.4. Phase-resolved spectral analysis

Taking advantage of the long, broadband HXMT observations, we also performed a pulse phase-resolved spectral analysis of the HXMT data. For this, 11 phase bins were chosen to pro-

Table 2. Best-fit parameters of the phase-averaged broadband spectrum of EXO 2030+375 as observed by IXPE, HXMT and ART-XC and obtained from spectro-polarimetric analysis using the model const×tbabs(powerlaw×highecut×polconst+gauss) in the 2–70 keV energy band.

Parameter	Value		
$N_{\rm H} [10^{22} \rm cm^{-2}]$	1.94 ± 0.03		
Γ	1.289 ± 0.006		
$Norm_{\Gamma}^{(a)}$	0.310 ± 0.004		
$E_{\rm cut}$ [keV]	5.8 ± 0.1		
$E_{ m fold}[{ m keV}]$	23.5 ± 0.3		
$E_{\mathrm{K}\alpha}$ [keV]	6.56 ± 0.02		
$\sigma_{\mathrm{K}\alpha}$ [keV]	0.24 ± 0.03		
$norm_{K\alpha}$ [ph cm ⁻² s ⁻¹]	0.0025 ± 0.0002		
PD [%]	1.2 ± 0.2		
PA [deg]	39 ± 8		
$C_{\rm DU1}$ (fixed)	1		
$C_{ m DU2}$	0.963 ± 0.001		
$C_{ m DU3}$	0.928 ± 0.001		
$C_{ m LE}$	1.400 ± 0.004		
$C_{ m ME}$	1.343 ± 0.004		
$C_{ m HE}$	1.255 ± 0.002		
$C_{ m ART-XC}$	1.395 ± 0.004		
$Flux_{1-70 \text{ keV}}^{(b)}$	4.44 ± 0.01		
χ^2 /d.o.f.	2448/2592		

Notes. All reported errors are at the 68% confidence level and based on the MCMC chain values. ^(a)Normalization of the power law in units of photon cm⁻² s⁻¹ keV⁻¹ at 1 keV. ^(b)Unabsorbed flux (in units of 10^{-9} erg cm⁻² s⁻¹) calculated for the entire model, obtained using the cflux command from XSPEC as resulting from the HXMT/LE data.

vide similar statistics of spectra in each bin. However, given the limited statistics with respect to phase-averaged analysis, we limited HXMT/HE data to 50 keV. To model the phase-resolved spectra, we used the same model employed for the phaseaveraged spectrum (see Sect. 3.2.2). The best-fit results are reported in Fig. 7. The analysis shows strong variability of the spectral parameters with pulse phase. We notice that the observed parameter variations might at least partly due to artificial correlations of degenerate parameters. We tested this through the calculation of contour plots for different pairs of parameters and verified that although the parameters show some intrinsic correlations, their variability is still significant. Although part of this variability is known to be model-dependent (Klochkov et al. 2008; Hemphill et al. 2014), it is nonetheless useful to test luminosity-dependence of the parameters variability with pulse phase (see Sect. 4.3).

4. Discussion

4.1. Polarization degree: Expectations versus observations

Our analysis shows a low polarization for the X-ray radiation from EXO 2030+375, with the phase-averaged PD in the 0%–3% range and the phase-resolved PD values in the range of 2%–7%. High values for the PD were expected from theoretical models of accreting XRPs (Caiazzo & Heyl 2021b,a, and references therein). This is due to both plasma and vacuum birefringence, which modify the opacity in the magnetic field depending on polarization of photons. Thus, emitted photons get polarized in two normal modes, namely: ordinary (O) and extraordinary

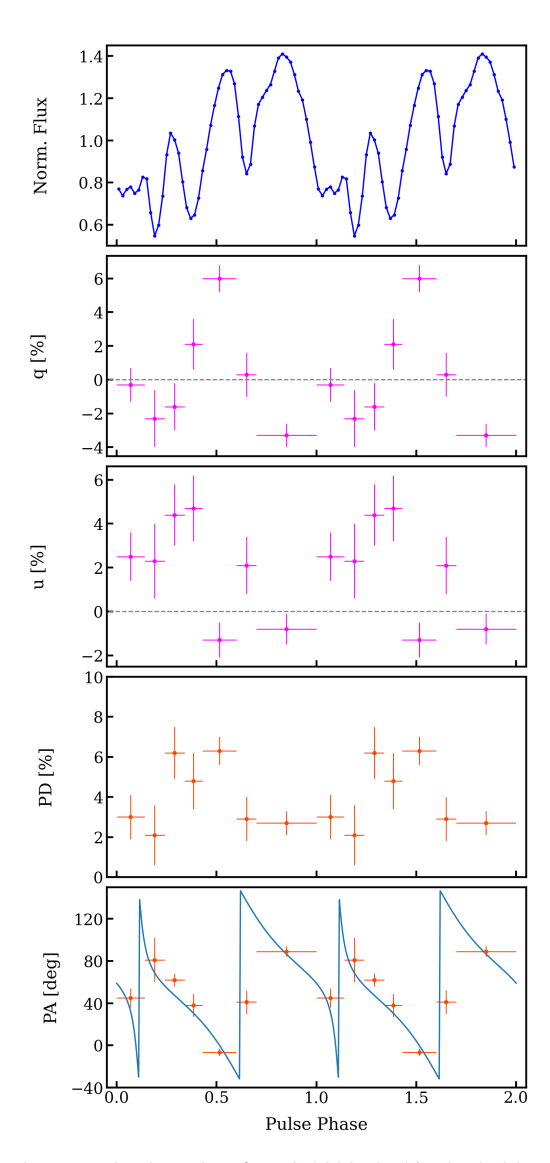


Fig. 6. Phase-resolved results of EXO 2030+375 in the 2–8 keV range, combining data from all IXPE DUs. From top to bottom, we show the pulse profile, normalized Stokes parameters q and u based on the polarimetric analysis, and the PD and PA, as obtained from the spectropolarimetric analysis. The blue line in the PA panel corresponds to the best-fit rotating vector model (see Sect. 4.2).

(X), representing oscillations of the electric field parallel and perpendicular to the plane formed by the local magnetic field and the photon momentum, respectively.

Recently, however, those models have been challenged by IXPE observations of several accreting XRPs, namely: Her X-1 (Doroshenko et al. 2022), Cen X-3 (Tsygankov et al. 2022), 4U 1626–67 (Marshall et al. 2022), Vela X-1 (Forsblom et al. 2023), and GRO J1008–57 (Tsygankov et al. 2023). In fact, all those sources show a far lower PD than expected. The observed relatively low polarization was interpreted in terms of a "vacuum resonance" occurring where the contributions from plasma and vacuum are equal (Lai & Ho 2002). Passing through the resonance, ordinary and extraordinary polarization modes of X-ray photons would convert to each other, with a net effect of depolarizing the radiation. This process takes place at a plasma density $\rho_V \approx 10^{-4} B_{12}^2 E_{\rm keV}^2 {\rm g \, cm}^{-3}$, where B_{12} is the magnetic field strength in units of $10^{12} {\rm G}$ and $E_{\rm keV}$ is the photon energy in keV. Doroshenko et al. (2022) found that a transition layer of

about $3\,\mathrm{g\,cm^{-2}}$ (corresponding to a Thomson optical depth of about unity) would depolarize the observed radiation consistently with the measured polarimetric quantities – if the vacuum resonance is located in the overheated atmospheric layer, which happens in the sub-critical (or low-) accretion regime. With the 2–10 keV flux of $2.5\times10^{-9}\,\mathrm{erg\,cm^{-2}\,s^{-1}}$ (see Table 1) and at a distance of $2.4\,\mathrm{kpc}$, the observed source luminosity is $2\times10^{36}\,\mathrm{erg\,s^{-1}}$. This luminosity value is comparable to the low luminosity state of Cen X-3 (Tsygankov et al. 2022) and to the bright state of GRO J1008–57 (Tsygankov et al. 2023), as observed by IXPE. The former also shows no significant polarization in the phase-averaged analysis, while the latter shows significant polarization of about 4%. Therefore, it is possible that some other mechanisms beyond those linked to the accretion luminosity are responsible for the observed polarization degree.

One qualitative interpretation of the observed low PD is pointed by the complex pulse profile of EXO 2030+375 (see Figs. 6 and 7). Such a complexity may derive from a complex magnetic field geometry where different hot spots simultaneously contribute to the observed emission at different pulse phases. The observed low PD might therefore be interpreted as due to mixing of emission from several parts of NS surface observed at different angles.

Another interpretation can be linked to the relation between the magnetic field geometry, in particular, the magnetic obliquity and the observer's line of sight. If the magnetic dipole is nearly aligned with the rotation axis and the observer looks from the side (as seems to be the case for Her X-1 and Cen X-3), the changes in the PA with the pulsar phase are rather small and the average polarization is significant. On the other hand, for a highly inclined dipole (especially when observed at small inclinations), the variations of the dipole position angle (that is reflected in the PA) are large, resulting in a strongly reduced average polarization. This interpretation is in line with the results obtained for the system geometry in EXO 2030+375 and further discussed in the next section.

4.2. Geometry of the system

The polarimetric quantity PA can be exploited to constrain the geometry of the system by fitting the unbinned polarimetric measurements from individual photoelectric angles with the rotating-vector model (RVM, Radhakrishnan & Cooke 1969; Poutanen 2020). If radiation escapes in the *O*-mode, the RVM describes the PA as follows:

$$\tan(\text{PA} - \chi_{\text{p}}) = \frac{-\sin\theta \sin(\phi - \phi_0)}{\sin i_{\text{p}}\cos\theta - \cos i_{\text{p}}\sin\theta\cos(\phi - \phi_0)},$$
 (1)

where i_p is the pulsar inclination (the angle between the pulsar spin vector and the line of sight), χ_p is the position angle (measured from north to east) of the pulsar spin, θ is the magnetic obliquity (the angle between the magnetic dipole and the spin axis), ϕ is the pulse phase, and ϕ_0 is the phase when the northern magnetic pole is closest to the observer. The other pole makes its closest approach half a period later. Using the RVM fit to the unbinned Stokes parameters on a photon-by-photon basis (González-Caniulef et al. 2023) and running Markov chain Monte Carlo (MCMC) simulations, we obtained estimates of the pulsar inclination, namely: $i_p = 129^{+9}_{-7}$ deg, along with the co-latitude of the magnetic pole (or magnetic obliquity), $\theta = 59^{+5}_{-6}$ deg, and the position angle of the pulsar spin, $\chi_p = \chi_{p,O} = -30 \pm 5$ deg (see Fig. 8). With the pulsar inclination and magnetic obliquity angles being almost supplementary, $i_p + \theta \approx 180^\circ$,

Table 3. Best-fit results of the spectro-polarimetric analysis of the phase-resolved IXPE data of EXO 2030+375 using the const×tbabs(powerlaw×polconst) model in the 2–8 keV energy band.

Phase	$N_{\rm H}$ $(10^{22}{\rm cm}^{-2})$	Γ	Norm (a)	PD (%)	PA (deg)	χ^2 /d.o.f.
0.00-0.18	2.9 ± 0.1	1.42 ± 0.02	4.9 ± 0.2	3.0 ± 1.1	45 ± 9	991/1037
0.18-0.26	3.2 ± 0.2	1.53 ± 0.04	2.3 ± 0.1	2.1 ± 1.5	81 ± 21	1015/1098
0.26-0.35	3.4 ± 0.1	1.44 ± 0.03	3.2 ± 0.1	6.2 ± 1.3	62 ± 6	938/974
0.35-0.44	2.3 ± 0.1	1.07 ± 0.03	1.4 ± 0.1	4.8 ± 1.5	38 ± 11	754/788
0.44-0.63	3.34 ± 0.09	1.17 ± 0.02	6.4 ± 0.2	6.3 ± 0.7	-6.5 ± 3.3	878/905
0.63-0.72	2.5 ± 0.1	$1.22 \pm 0.03 \\ 1.30 \pm 0.02$	2.4 ± 0.1	2.9 ± 1.1	41 ± 11	1009/1048
0.72-1.00	3.06 ± 0.07		10.9 ± 0.2	2.7 ± 0.6	89 ± 5	1103/1222

Notes. All reported errors are at 68% confidence level. (a) Normalization of the power law in units of 10^{-2} photon keV⁻¹ cm⁻² s⁻¹ at 1 keV as obtained from DU1.

the southern magnetic pole swings close to the observer line of sight at each pulsar rotation at half a period from phase $\phi_0/(2\pi)$, that is: at $\phi = 0.11^{+0.02}_{-0.01}$.

Interestingly, in the case of EXO 2030+375 the RVM suggests a relatively high magnetic obliquity. Other XRPs (e.g., Her X-1, Cen X-3) show $\theta \approx 15^\circ$, while a value of $\theta \approx 60^\circ$ observed from EXO 2030+375 is closer to the orthogonal rotator GRO J1008-57 (Tsygankov et al. 2023). These results indicate that EXO 2030+375 stands in between the bimodal distribution peaking at 0° and 90° of the magnetic obliquity expected for isolated NSs (Dall'Osso & Perna 2017; Lander & Jones 2018), although such results do not necessarily apply to accreting XRPs (Biryukov & Abolmasov 2021).

The orbital inclination can be obtained from the orbital parameters measured by Wilson et al. (2008). For the optical companion stellar mass in the range $17-20\,M_\odot$, corresponding to B0V spectral class (Coe et al. 1988), and assuming a NS mass of $1.4\,M_\odot$, the inclination is in the range $49^\circ-55^\circ$ (see also Laplace et al. 2017). This value is consistent with the pulsar inclination value derived through the RVM fit because the sense of rotation cannot be determined from the X-ray pulse arrival times (i.e., solutions in the range $i_{\rm orb}=125^\circ-131^\circ$ are equally probable).

4.3. HXMT phase-resolved spectral results

Spectral parameters are expected to show pulse phase-dependence due to the highly anisotropic accretion geometry in XRPs. We therefore performed phase-resolved spectroscopy of HXMT EXO 2030+375 data (see Fig. 7). Phase-resolved spectroscopy of EXO 2030+375 was also performed in earlier works (Klochkov et al. 2008; Naik & Jaisawal 2015; Tamang et al. 2022). However, despite the main continuum model used in past works is similar to the one adopted here, several important differences prevent a direct comparison. In fact, XRP spectra are known to be luminosity-dependent (Mushtukov & Tsygankov 2022) and, as a consequence, different spectral components can be adopted to fit the data collected at different luminosity levels.

For EXO 2030+375, the main continuum model was modified in different works with additional components such as a Gaussian absorption line around 10 keV (Klochkov et al. 2008) or a partial covering component (Naik & Jaisawal 2015; Tamang et al. 2022). Therefore, only a qualitative comparison can be made between the results obtained here and those from previous works. For example, observations carried out by Klochkov et al. (2008) of EXO 2030+375 show that the power-law photon index reaches a minimum around the main pulse

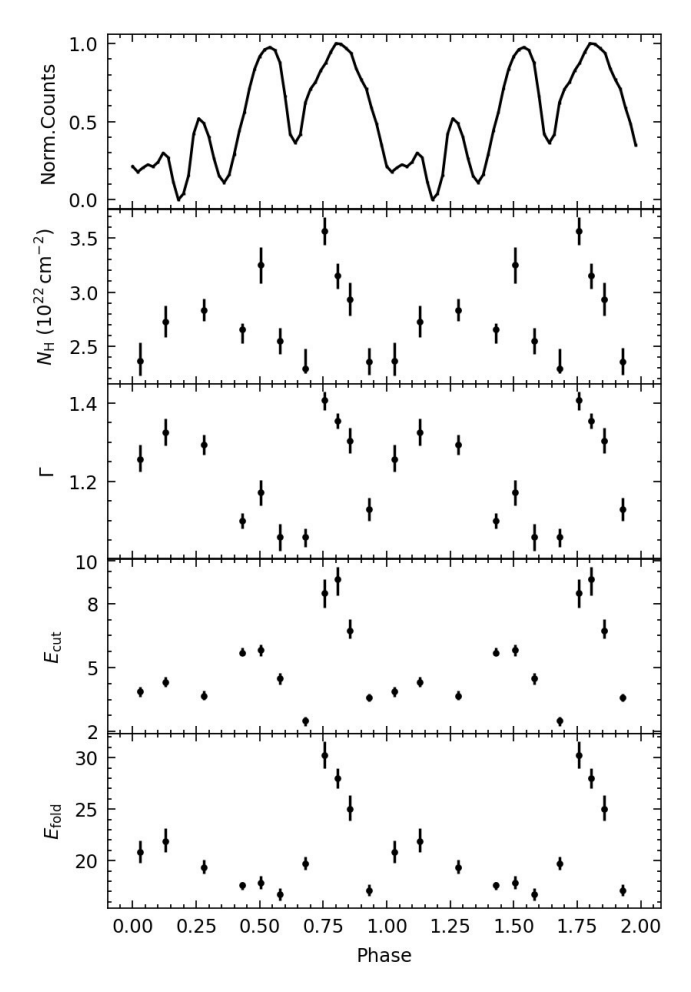


Fig. 7. Best-fit parameters for the broadband (2–50 keV) phase-resolved spectra of EXO 2030+375 as observed by HXMT. Panels from top to bottom show the pulse profile as observed by HXMT/LE in the 2–10 keV energy band; the column density, $N_{\rm H}$; the power-law photon index Γ ; the cutoff energy; and the folding energy (both in keV).

profile peak (corresponding to the broad main peak at $\phi \sim 0.8$ in Fig. 7). A similar trend has emerged also from the phase-resolved results observed in Her X-1 (Vasco et al. 2013). Here, in contrast, we observe a maximum value of the photon index around the same peak (see Fig. 7). This is likely a consequence of the luminosity difference, as the above-mentioned works derive their results in the high-luminosity accretion regime

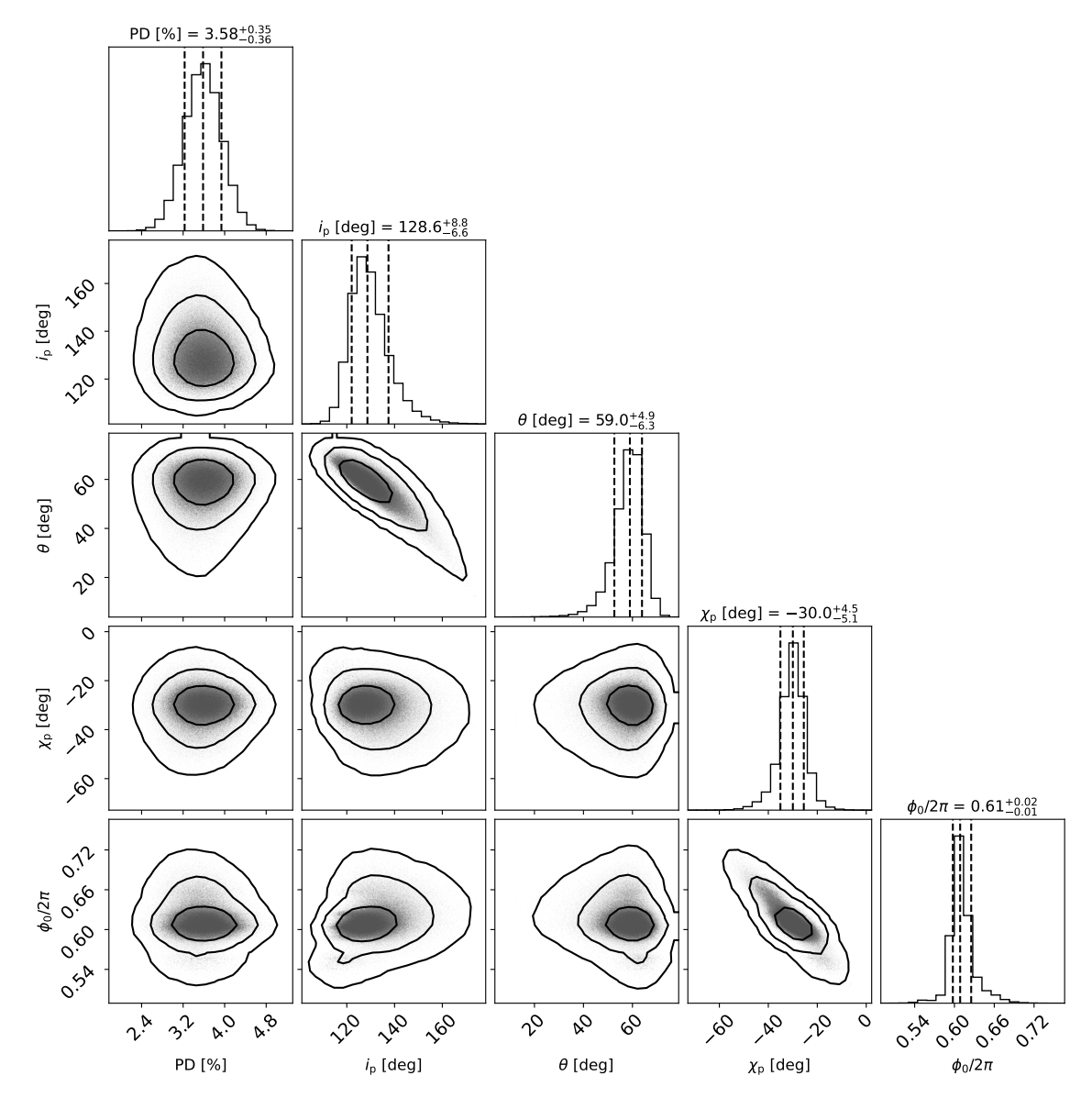


Fig. 8. Corner plot of the posterior distribution for the RVM parameters for the pulsar geometry obtained using the PA values. Parameters are the PD of radiation escaping from the magnetic pole, pulsar inclination, i_p ; magnetic obliquity, θ ; position angle, χ_p ; and the phase, ϕ_0 . 2D contours correspond to 68%, 95% and 99% confidence levels. The histograms show the normalized 1D distribution for a given parameter derived from the posterior samples. The mean value and 1σ confidence levels for the derived parameters are reported above the corresponding histogram.

 $(10^{37-38} \,\mathrm{erg}\,\mathrm{s}^{-1})$, that is near or above the critical luminosity), whereas in the present work the source has been observed at sub-critical luminosity ($\sim 4 \times 10^{36} \,\mathrm{erg \, s^{-1}}$). Such a difference is reflected in two main aspects. On the one side, the accretion structure beaming pattern is expected to drastically change at different regimes. In fact, the EXO 2030+375 pulse profile observed in the high-luminosity regime (see, e.g., the 2–9 keV panel in Fig. 2 of Klochkov et al. 2008) exhibits substantial differences with what is observed in the present work (see top panel in Fig. 7). This can lead to opposite observational signatures if the observer looks through the optically deep walls of the accretion column in the super-critical regime or through the optically thin hot-spots in the sub-critical regime (Mushtukov et al. 2015; Becker & Wolff 2022). On the other hand, opposite luminositydependences of spectral parameters have been observed in different accretion regimes in XRPs, depending on whether a gas-mediated or a radiation-dominated shock is responsible for the infalling plasma deceleration (Klochkov et al. 2011, and references therein). Although such behavior has generally been observed in the pulse-averaged analysis (see, e.g., Müller et al. 2013; Reig & Nespoli 2013; Malacaria et al. 2015; Diez et al. 2022), pulse-to-pulse spectroscopy hints at the possibility that similar trends are at work on shorter timescales (Klochkov et al. 2011; Vybornov et al. 2017; Müller et al. 2013) and that even phase-resolved spectroscopy exhibits a pulse-phase dependence of most parameters on luminosity (Lutovinov et al. 2016).

The system geometry derived in Sect. 4.2 shows that the southern magnetic pole swings close to the observer line of sight at phase 0.1 (that is, half a period from ϕ_0). As the observation is carried out at sub-critical accretion, an accretion column with emitting walls contributing at neighbor phases is not expected. Thus, the main pulse profile peak at phase 0.8 is perhaps due to light bending from pencil beam emission at the magnetic poles. Such emission is generated in an optically thin environment at the hot-spot and it is therefore intrinsically soft, leading to a maximum of the photon index. However, this

scenario would likely produce a symmetrical behavior of the spectral parameters dependence around the phase ϕ_0 , which is not observed here. This result, together with the highly-structured pulse profile, hints to a more complex NS configuration, such as a multipolar or asymmetric topology of the magnetic field. This kind of magnetic field configuration has also been recently proposed for other XRPs (Postnov et al. 2013; Tsygankov et al. 2017; Israel et al. 2017; Mönkkönen et al. 2022).

5. Summary

Our main results can be summarized as follows:

- EXO 2030+375 was observed in November 2022 by IXPE, HXMT and ART-XC at the peak of a low-luminosity Type I outburst.
- Only a low polarization degree of 0%-3% has been found in the phase-averaged analysis, while the phase-resolved analysis reveals a PD in the range of 2%-7%.
- The observed low PD can be explained in terms of an overheated NS atmosphere scenario, with additional depolarizing mechanisms possibly at work in EXO 2030+375. We propose that mixing of emission from several parts of the NS surface observed at different angles, on one hand, and variations of the dipole position angle resulting in changes in the PA on the other, would lead to further depolarization.
- By means of the rotating vector model, we constrained the geometry of the accreting pulsar. The pulsar inclination is $\sim 130^{\circ}$, almost supplementary to the magnetic obliquity angle, at $\sim 60^{\circ}$ (that is, their sum is $\sim 180^{\circ}$). The obtained pulsar geometry implies that the magnetic axis swings close to the observer line of sight and the system obliquity stands between orthogonal and aligned rotators.
- The spectral phase-resolved analysis shows evidence that the pulse phase dependence of spectral parameters is different for different luminosities. This possibly reflects changes in the accretion structure at different accretion regimes, accompanied by beam pattern changes.
- Polarimetric, spectral, and timing analyses all hint toward a complex accretion geometry, where magnetic multipoles with asymmetric topology and gravitational light bending have significant effects on the resulting spectral and timing behavior of EXO 2030+375.

Our analysis of EXO 2030+375 characterized the X-ray polarimetric and spectral properties of the source at the sub-critical accretion regime. Additional future observations at different luminosities would help discerning the various mechanisms at work that shape the X-ray emission properties.

Acknowledgements. The Imaging X-ray Polarimetry Explorer (IXPE) is a joint US and Italian mission. The US contribution is supported by the National Aeronautics and Space Administration (NASA) and led and managed by its Marshall Space Flight Center (MSFC) with industry partner Ball Aerospace (contract NNM15AA18C). The Italian contribution is supported by the Italian Space Agency (Agenzia Spaziale Italiana, ASI) through contract ASI-OHBI-2017-12-I.0, agreements ASI-INAF-2017-12-H0 and ASI-INFN-2017.13-H0, and its Space Science Data Center (SSDC) with agreements ASI-INAF-2022-14-HH.0 and ASI-INFN 2021-43-HH.0, and by the Istituto Nazionale di Astrofisica (INAF) and the Istituto Nazionale di Fisica Nucleare (INFN) in Italy. This research used data products provided by the IXPE Team (MSFC, SSDC, INAF, and INFN) and distributed with additional software tools by the High-Energy Astrophysics Science Archive Research Center (HEASARC), which is a service of the Astrophysics Science Division at NASA/GSFC and the High Energy Astrophysics Division of the Smithsonian Astrophysical Observatory. We acknowledge extensive use of the NASA Abstract Database Service (ADS). This research was supported by the International Space Science Institute (ISSI) in Bern, through ISSI International Team project 495. JH acknowledges support from the Natural Sciences and Engineering Research Council of Canada (NSERC) through a Discovery Grant, the Canadian Space Agency through the co-investigator grant program, and computational resources and services provided by Compute Canada, Advanced Research Computing at the University of British Columbia, and the SciServer science platform (www.sciserver.org). We also acknowledge support from the Academy of Finland grants 333112, 349144, 349373, and 349906 (SST, JP), the German Academic Exchange Service (DAAD) travel grant 57525212 (VD, VFS), the Väisälä Foundation (SST), the Russian Science Foundation grant 19-12-00423 (AAL, IAM, SVM, AES), the French National Centre for Scientific Research (CNRS), and the French National Centre for Space Studies (CNES) (POP). We thank Lingda Kong and Youli Tuo for their helpful assistance in the HXMT data analysis.

References

```
Arnaud, K. A. 1996, in Astronomical Data Analysis Software and Systems V,
   eds. G. H. Jacoby, & J. Barnes (San Francisco: ASP), ASP Conf. Ser., 101,
Bailer-Jones, C. A. L., Rybizki, J., Fouesneau, M., Demleitner, M., & Andrae,
   R. 2021, AJ, 161, 147
Baldini, L., Barbanera, M., Bellazzini, R., et al. 2021, Astropart. Phys., 133,
   102628
Baldini, L., Bucciantini, N., Lalla, N. D., et al. 2022, SoftwareX, 19, 101194
Becker, P. A., & Wolff, M. T. 2022, ApJ, 939, 67
Bellazzini, R., & Angelini, F. 2003, in Polarimetry in Astronomy, ed. S. Fineschi,
   Proc. SPIE, 4843, 383
Biryukov, A., & Abolmasov, P. 2021, MNRAS, 505, 1775
Caiazzo, I., & Heyl, J. 2021a, MNRAS, 501, 129
Caiazzo, I., & Heyl, J. 2021b, MNRAS, 501, 109
Coe, M. J., Longmore, A., Payne, B. J., & Hanson, C. G. 1988, MNRAS, 232,
Corbet, R. H. D., & Levine, A. M. 2006, ATel, 843, 1
Dall'Osso, S., & Perna, R. 2017, MNRAS, 472, 2142
Deeter, J. E., Boynton, P. E., & Pravdo, S. H. 1981, ApJ, 247, 1003
Diez, C. M., Grinberg, V., Fürst, F., et al. 2022, A&A, 660, A19
Di Marco, A., Costa, E., Muleri, F., et al. 2022, AJ, 163, 170
Di Marco, A., Soffitta, P., Costa, E., et al. 2023, AJ, 165, 143
Doroshenko, V., Poutanen, J., Tsygankov, S. S., et al. 2022, Nat. Astron., 6, 1433
Epili, P., Naik, S., Jaisawal, G. K., & Gupta, S. 2017, MNRAS, 472, 3453
Forsblom, S. V., Poutanen, J., Tsygankov, S. S., et al. 2023, ApJ, 947, L20
Fu, Y.-C., Song, L. M., Ding, G. Q., et al. 2023, MNRAS, 521, 893
Fürst, F., Falkner, S., Marcu-Cheatham, D., et al. 2018, A&A, 620, A153
Gehrels, N., Chincarini, G., Giommi, P., et al. 2004, ApJ, 611, 1005
Gnedin, Y. N., Pavlov, G. G., & Shibanov, Y. A. 1978, Sov. Astron. Lett., 4, 117
González-Caniulef, D., Caiazzo, I., & Heyl, J. 2023, MNRAS, 519, 5902
Hemphill, P. B., Rothschild, R. E., Markowitz, A., et al. 2014, ApJ, 792, 14
HI4PI Collaboration (Ben Bekhti, N., et al.) 2016, A&A, 594, A116
Israel, G. L., Belfiore, A., Stella, L., et al. 2017, Science, 355, 817
Kislat, F., Clark, B., Beilicke, M., & Krawczynski, H. 2015, Astropart. Phys., 68,
Klochkov, D., Santangelo, A., Staubert, R., & Ferrigno, C. 2008, A&A, 491, 833
Klochkov, D., Staubert, R., Santangelo, A., Rothschild, R. E., & Ferrigno, C.
   2011, A&A, 532, A126
Krimm, H. A., Holland, S. T., Corbet, R. H. D., et al. 2013, ApJS, 209, 14
Lai, D., & Ho, W. C. G. 2002, ApJ, 566, 373
Lander, S. K., & Jones, D. I. 2018, MNRAS, 481, 4169
Laplace, E., Mihara, T., Moritani, Y., et al. 2017, A&A, 597, A124
Li, X., Li, X., Tan, Y., et al. 2020, J. High Energy Astrophys., 27, 64
Lutovinov, A. A., Buckley, D. A. H., Townsend, L. J., Tsygankov, S. S., &
   Kennea, J. 2016, MNRAS, 462, 3823
Malacaria, C., Klochkov, D., Santangelo, A., & Staubert, R. 2015, A&A, 581,
   A121
Marshall, H. L., Ng, M., Rogantini, D., et al. 2022, ApJ, 940, 70
Meszaros, P., Novick, R., Szentgyorgyi, A., Chanan, G. A., & Weisskopf, M. C.
   1988, ApJ, 324, 1056
Mönkkönen, J., Tsygankov, S. S., Mushtukov, A. A., et al. 2022, MNRAS, 515,
Müller, D., Klochkov, D., Caballero, I., & Santangelo, A. 2013, A&A, 552, A81
Mushtukov, A., & Tsygankov, S. 2022, in Handbook of X-ray and Gamma-ray
   Astrophysics, eds. C. Bambi, & A. Santangelo (Singapore: Springer)
```

Mushtukov, A. A., Suleimanov, V. F., Tsygankov, S. S., & Poutanen, J. 2015,

Parmar, A. N., White, N. E., Stella, L., Izzo, C., & Ferri, P. 1989, ApJ, 338, 359

Pavlov, G. G., & Shibanov, Y. A. 1979, Sov. J. Exp. Theoret. Phys., 49, 741

Pavlinsky, M., Tkachenko, A., Levin, V., et al. 2021, A&A, 650, A42

Postnov, K., Shakura, N., Staubert, R., et al. 2013, MNRAS, 435, 1147

MNRAS, 447, 1847

Naik, S., & Jaisawal, G. K. 2015, RAA, 15, 537

Radhakrishnan, V., & Cooke, D. J. 1969, ApJ, 3, 225

Poutanen, J. 2020, A&A, 641, A166

- Reig, P., & Coe, M. J. 1998, MNRAS, 294, 118 Reig, P., & Nespoli, E. 2013, A&A, 551, A1
- Silvestri, S., & IXPE Collaboration 2023, Nucl. Instrum. Methods Phys. Res. A, 1048, 167938
- Soffitta, P., Baldini, L., Bellazzini, R., et al. 2021, AJ, 162, 208 Strohmayer, T. E. 2017, ApJ, 838, 72
- Sunyaev, R., Arefiev, V., Babyshkin, V., et al. 2021, A&A, 656, A132 Tamang, R., Ghising, M., Tobrej, M., Rai, B., & Paul, B. C. 2022, MNRAS, 515,
- Thalhammer, P., Ballhausen, R., Pottschmidt, K., et al. 2021, ATel, 14911, 1Tsygankov, S. S., Doroshenko, V., Lutovinov, A. A., Mushtukov, A. A., & Poutanen, J. 2017, A&A, 605, A39
- Tsygankov, S. S., Doroshenko, V., Poutanen, J., et al. 2022, ApJ, 941, L14
 Tsygankov, S. S., Doroshenko, V., Mushtukov, A. A., et al. 2023, A&A, in press https://doi.org/10.1051/0004-6361/202346134
- Vasco, D., Staubert, R., Klochkov, D., et al. 2013, A&A, 550, A111 Vybornov, V., Klochkov, D., Gornostaev, M., et al. 2017, A&A, 601, A126 Weisskopf, M. C., Soffitta, P., Baldini, L., et al. 2022, JATIS, 8, 026002 Wenger, M., Ochsenbein, F., Egret, D., et al. 2000, A&AS, 143, 9 Wilms, J., Allen, A., & McCray, R. 2000, ApJ, 542, 914

Wilson, C. A., Finger, M. H., & Camero-Arranz, A. 2008, ApJ, 678, 1263
Zhang, S.-N., Li, T., Lu, F., et al. 2020, Sci. China Phys. Mech. Astron., 63, 249502

- ¹ International Space Science Institute, Hallerstrasse 6, 3012 Bern, Switzerland
- e-mail: cmalacaria.astro@gmail.com University of British Columbia, Vancouver, BC V6T 1Z4, Canada
- ³ Institut für Astronomie und Astrophysik, Universität Tübingen, Sand 1, 72076 Tübingen, Germany
- Department of Physics and Astronomy, University of Turku, 20014 Turku, Finland
- ⁵ INAF Istituto di Astrofisica e Planetologia Spaziali, Via del Fosso del Cavaliere 100, 00133 Roma, Italy
- 6 ISDC Data Center for Astrophysics, Université de Genève, 16 chemin d'Écogia, 1290 Versoix, Switzerland
- ⁷ Space Research Institute (IKI) of Russian Academy of Sciences, Prosoyuznaya ul 84/32, 117997 Moscow, Russian Federation
- MIT Kavli Institute for Astrophysics and Space Research, Massachusetts Institute of Technology, 77 Massachusetts Avenue, Cambridge, MA 02139, USA
- ⁹ Astrophysics, Department of Physics, University of Oxford, Denys Wilkinson Building, Keble Road, Oxford OX1 3RH, UK
- ¹⁰ Université Grenoble Alpes, CNRS, IPAG, 38000 Grenoble, France
- ¹¹ Instituto de Astrofísicade Andalucía CSIC, Glorieta de la Astronomía s/n, 18008 Granada, Spain
- ¹² INAF Osservatorio Astronomico di Roma, Via Frascati 33, 00040 Monte Porzio Catone, RM, Italy
- Space Science Data Center, Agenzia Spaziale Italiana, Via del Politecnico snc, 00133 Roma, Italy
- INAF Osservatorio Astronomico di Cagliari, Via della Scienza 5,
 09047 Selargius, CA, Italy
- Istituto Nazionale di Fisica Nucleare, Sezione di Pisa, Largo B. Pontecorvo 3, 56127 Pisa, Italy
- Dipartimento di Fisica, Università di Pisa, Largo B. Pontecorvo 3, 56127 Pisa, Italy
- NASA Marshall Space Flight Center, Huntsville, AL 35812, USA
- Dipartimento di Matematica e Fisica, Università degli Studi Roma Tre, Via della Vasca Navale 84, 00146 Roma, Italy
- ¹⁹ Istituto Nazionale di Fisica Nucleare, Sezione di Torino, Via Pietro Giuria 1, 10125 Torino, Italy
- Dipartimento di Fisica, Università degli Studi di Torino, Via Pietro Giuria 1, 10125 Torino, Italy
- ²¹ INAF Osservatorio Astrofisico di Arcetri, Largo Enrico Fermi 5, 50125 Firenze, Italy
- ²² Dipartimento di Fisica e Astronomia, Università degli Studi di Firenze, Via Sansone 1, 50019 Sesto Fiorentino, FI, Italy

- ²³ Istituto Nazionale di Fisica Nucleare, Sezione di Firenze, Via Sansone 1, 50019 Sesto Fiorentino, FI, Italy
- ²⁴ Agenzia Spaziale Italiana, Via del Politecnico snc, 00133 Roma, Italy
- ²⁵ Science and Technology Institute, Universities Space Research Association, Huntsville, AL 35805, USA
- ²⁶ Istituto Nazionale di Fisica Nucleare, Sezione di Roma "Tor Vergata", Via della Ricerca Scientifica 1, 00133 Roma, Italy
- ²⁷ Department of Physics and Kavli Institute for Particle Astrophysics and Cosmology, Stanford University, Stanford, CA 94305, USA
- Astronomical Institute of the Czech Academy of Sciences, Bocní- II 1401/1, 14100 Praha 4, Czech Republic
- ²⁹ RIKEN Cluster for Pioneering Research, 2-1 Hirosawa, Wako, Saitama 351-0198, Japan
- California Institute of Technology, Pasadena, CA 91125, USA
- Yamagata University, 1-4-12 Kojirakawa-machi, Yamagata-shi 990-8560, Japan
- ³² Osaka University, 1-1 Yamadaoka, Suita, Osaka 565-0871, Japan
- ³³ International Center for Hadron Astrophysics, Chiba University, Chiba 263-8522, Japan
- ³⁴ Institute for Astrophysical Research, Boston University, 725 Commonwealth Avenue, Boston, MA 02215, USA
- Department of Astrophysics, St. Petersburg State University, Universitetsky pr. 28, Petrodvoretz 198504, St. Petersburg, Russia
- ³⁶ Department of Physics and Astronomy and Space Science Center, University of New Hampshire, Durham, NH 03824, USA
- ³⁷ Physics Department and McDonnell Center for the Space Sciences, Washington University in St. Louis, St. Louis, MO 63130, USA
- ³⁸ Finnish Centre for Astronomy with ESO, University of Turku, 20014 Turku, Finland
- ³⁹ Istituto Nazionale di Fisica Nucleare, Sezione di Napoli, Strada Comunale Cinthia, 80126 Napoli, Italy
- ⁴⁰ Université de Strasbourg, CNRS, Observatoire Astronomique de Strasbourg, UMR 7550, 67000 Strasbourg, France
- ⁴¹ Graduate School of Science, Division of Particle and Astrophysical Science, Nagoya University, Furo-cho, Chikusa-ku, Nagoya, Aichi 464-8602, Japan
- ⁴² Hiroshima Astrophysical Science Center, Hiroshima University, 1-3-1 Kagamiyama, Higashi-Hiroshima, Hiroshima 739-8526, Japan
- 43 University of Maryland, Baltimore County, Baltimore, MD 21250,
- ⁴⁴ NASA Goddard Space Flight Center, Greenbelt, MD 20771, USA
- 45 Center for Research and Exploration in Space Science and Technology, NASA/GSFC, Greenbelt, MD 20771, USA
- Department of Physics, University of Hong Kong, Pokfulam,
 Hong Kong
- ⁴⁷ Department of Astronomy and Astrophysics, Pennsylvania State University, University Park, PA 16801, USA
- ⁴⁸ Center for Astrophysics, Harvard & Smithsonian, 60 Garden St, Cambridge, MA 02138, USA
- ⁴⁹ INAF Osservatorio Astronomico di Brera, Via E. Bianchi 46, 23807 Merate, LC, Italy
- ⁵⁰ Dipartimento di Fisica e Astronomia, Università degli Studi di Padova, Via Marzolo 8, 35131 Padova, Italy
- ⁵¹ Dipartimento di Fisica, Università degli Studi di Roma "Tor Vergata", Via della Ricerca Scientifica 1, 00133 Roma, Italy
- Department of Astronomy, University of Maryland, College Park, Maryland 20742, USA
- 53 Mullard Space Science Laboratory, University College London, Holmbury St Mary, Dorking, Surrey RH5 6NT, UK
- Anton Pannekoek Institute for Astronomy & GRAPPA, University of Amsterdam, Science Park 904, 1098, XH Amsterdam, The Netherlands
- 55 Guangxi Key Laboratory for Relativistic Astrophysics, School of Physical Science and Technology, Guangxi University, Nanning 530004, PR China